Optimized Design of a Coupled-Inductor Buck Converter, 48 to 12 V, 1 kW, Using Planar Magnetics and GaN-FETs for MHz-Range Operation

Track 6. Vehicle Electrification-related Technologies

***Abstract*—The next generation of automotive vehicles and datacenters requires highly compact and efficient 48 V to 12 V point-of-load converters. This paper investigates the impact of coupling on the electrical properties of 2-phase buck converters operating in triangular current mode to achieve soft-switching. A novel planar inductor geometry with four poles and distributed air-gaps for operation beyond 1 MHz is presented that minimizes copper-losses from external proximity effect. An experimental prototype with 1 kW output achieves an impressive power density of 80 kW/l (1300 W/in³) and a peak efficiency of 96.3%, demonstrating the efficacy of the inductor structure.**

***Index Terms*—coupled inductor, magnetic integration, planar inductor, triangular current mode**

I. Introduction

With a growing power demand, power distribution in both conventional and electric vehicles presents an increasing challenge. Traditionally, 12 V are used to distribute the power to all auxiliary devices which requires large cable diameters. Moving to a 48 V distribution bus reduces the cost of the wire assembly and losses [1]. As most devices are still operating at 12 V, highly compact and efficient point-of-load converters are required. This conversion stage is a critical part of distributed power architectures and its performance has a direct impact on system-level efficiency, thermal design, and overall build volume.

With the rise of Gallium Nitride (GaN) power devices, operating converters in the MHz-range has become feasible, significantly reducing the size of the magnetic components [2]. At such high frequencies, hard-switched converters are inapt due to their large turn-on losses. Utilizing soft-switching, those losses are eliminated which allows operation in the MHz-range at excellent efficiencies [3]. Resonant converters inherently operate in soft-switching but are unsuitable when a regulated output voltage is required over a wide input voltage range. Traditional non-isolated converters such as buck or boost can also operate with soft-switching utilizing triangular current mode (TCM) as explained in the next section and only the small turn-on losses remain [4]. In soft-switched converters, magnetic components are often the main contributor to losses. Planar magnetics that use printed circuit board (PCB) windings are well-suited for those applications as they allow elaborate winding structures, effective cooling due to the large area per volume and direct integration with the other circuitry [5]–[8]. Lots of research was conducted for planar transformers but the design of compact and efficient planar inductors has its unique challenges due to the missing possibility for interleaving, the fringing of the air-gap and the DC-bias in the core. Utilizing multi-phase converters with coupled inductors is an effective way to reduce the volume and loss of the planar inductors as the flux can cancel out in certain areas [9].

In this paper, a 1 kW 2-phase coupled inductor buck converter for 48 to 12 V conversion is studied. To minimize the overall volume, a target switching-frequency range of 1 to 3 MHz was selected. Compared to previous work [5], [9]–[12], the low operating voltage requires a very low inductance whose design becomes particularly challenging due to the large phase current of 40 A and consequently over 80 A of ripple. Firstly, the effects of coupling on the electrical parameters are analyzed mathematically. Afterwards, different geometries for the single-turn inductor are optimized using a novel winding geometry and dual air-gaps. The most promising geometry based on the four-pole structure is implemented in an experimental prototype.

II. Coupled inductor buck converter in TCM

A. Working principle

The topology of the two phase coupled-inductor buck converter is shown in Figure 1. It operates like a conventional two-phase buck with both legs are switched 180° out of phase. When the leg 2 is pulled high, the current in leg 1 is also affected as shown in Figure 2: For positive coupling, the falling slope is steepened while for negative coupling it is flattened. The converter operates at very high ripple, more than twice the phase current such that the leg current

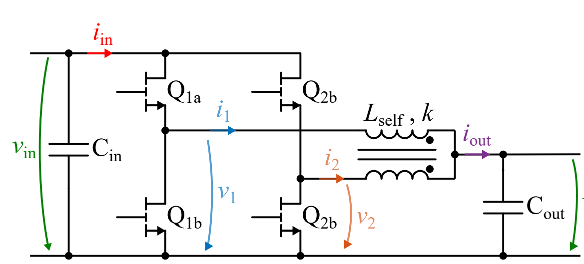

Fig. 1: Schematic of the Coupled Inductor Buck Converter.

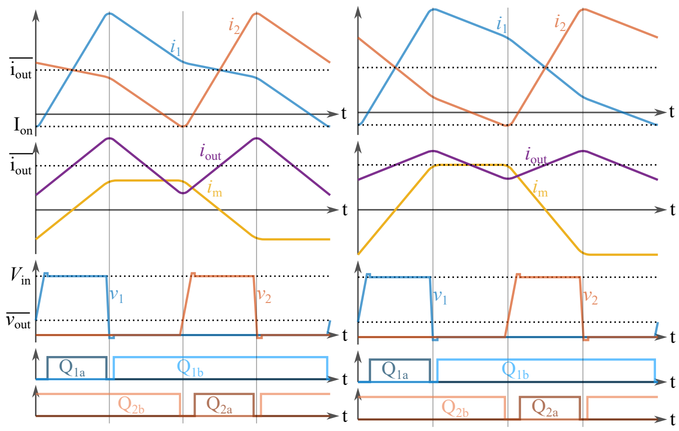

(a) Negative Coupling (b) Positive Coupling

Fig. 2: Waveforms for positive and negative coupling; dead-times are exaggerated. It can be seen that the slopes are changed but the behavior in the vicinity of the switching instances is fundamentally the same.

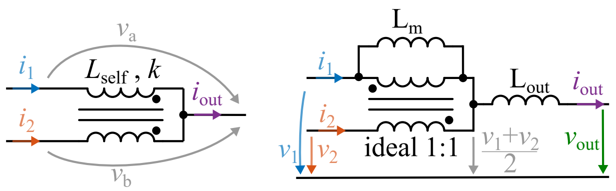

(a) Coupled Inductor (b) Transformer Model

Fig. 3: The coupled inductor can be described with a self-inductance $L_{\rm self}$ and coupling factor k or by using an equivalent circuit consisting of an ideal 1:1 transformer with magnetizing inductance $L_{\rm m}$ and common output inductance $L_{\rm out}$.

becomes negative prior to the rising edge of each leg resulting in a zero voltage switching (ZVS) turn-on of all transistors. This mode is called TCM. Only the small turn-off losses are observed now [4]. If the dead-time is too long, the devices enter reverse-conduction creating additional losses as shown in 2. In practice, these reverse-conduction losses can be almost eliminated by properly adjusting the dead-time.

B. Impact of the Coupling Factor

The symmetrical coupled inductor consists of two identical coils that are wound in a way, that the flux of one coil links with the flux of the second coil and vice versa with both coils connected on one side. This configuration can be described mathematically using

$$\begin{bmatrix} v_{\rm a} \\ v_{\rm b} \end{bmatrix} = \begin{bmatrix} 1 & k \\ k & 1 \end{bmatrix} L_{\rm self} \begin{bmatrix} \frac{di_1}{dt} \\ \frac{di_2}{dt} \end{bmatrix} \tag{1}$$

with self-inductance $L_{\rm self}$ and coupling-factor k. Note that k can be positive or negative; the impact of that will be analyzed later. In order to simplify the equations and provide a more intuitive understanding, the equivalent circuit in Figure 3b) is introduced. Both circuits are electrically equivalent for

$$\begin{aligned} L_{\rm out} &= (1+k)\frac{L_{\rm self}}{2} \\ L_{\rm m} &= (1-k)\frac{L_{\rm self}}{2}. \end{aligned} \tag{2}$$

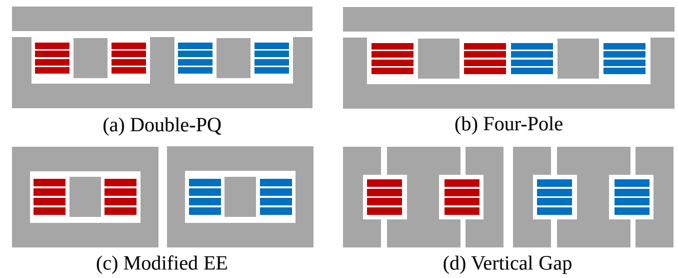

(a) Double-PQ (b) Four-Pole (c) Modified EE (d) Vertical Gap

Fig. 4: Structure of the cores in side-view if cut through the center. First winding in red, second winding in blue.

The voltage at the virtual central node in the transformer model is only dependent on the two leg voltages v_1 and v_2 decoupling the governing equations:

$$\begin{aligned} \frac{di_{\rm out}}{dt} &= \frac{1}{L_{\rm out}}\left(\frac{v_1+v_2}{2} - v_{\rm out}\right) \\ \frac{di_{\rm m}}{dt} &= \frac{1}{L_{\rm out}}\left(\frac{v_1-v_2}{2}\right) \\ \text{with} \quad i_{\rm out} &= i_1 + i_2 \quad \text{and} \quad i_{\rm m} = i_1 - i_2 \end{aligned} \tag{3}$$

From this, the differential equations for each interval can be easily calculated and equations for the important converter parameters can be derived. An effective dutycycle $D_{\rm eff}$ is introduced with $D_{\rm eff} = D$ for $D \leq 0.5$ and $D_{\rm eff} = 1 - D$ for $D > 0.5$ to create universal equations. The peak-to-peak output ripple is then given by

$$\Delta I_{\rm out} = \frac{2V_{\rm in}}{f_{\rm s}(1+k)L_{\rm self}} D_{\rm eff}\left(\frac{1}{2} - D_{\rm eff}\right). \tag{4}$$

The peak-to-peak ripple in each leg which is important for soft-switching is

$$\Delta I_{\rm leg} = \frac{V_{\rm in} D_{\rm eff}}{2 f_{\rm s} L_{\rm self}}\left(\frac{2}{1+k}\left(\frac{1}{2} - D_{\rm eff}\right) + \frac{1}{1-k}\right). \tag{5}$$

As mentioned before, for soft-switching $I_{\rm on}$ needs to be negative and generally needs to be below a certain value to guarantee a sufficiently short dead time which can be written as $\Delta I_{\rm leg} \geq \overline{i_{\rm out}} + 2I_{\rm on,max}$. This is fulfilled for

$$f_{\rm s} < \frac{V_{\rm in} D_{\rm eff}}{2L_{\rm self}(\overline{i_{\rm out}} + 2I_{\rm on,max})}\left(\frac{2}{1+k}\left(\frac{1}{2} - D_{\rm eff}\right) + \frac{1}{1-k}\right). \tag{6}$$

III. Inductor Design

a) Inductor geometry: Four different geometries, two coupled, and two uncoupled ones, were compared for this work as shown in Figure 4. The Double-PQ structure was originally introduced by [5] and basically combines two EQ-cores placed next to each other. The four-pole structure is very similar but omits the central pole which creates separate paths for common-mode and differential-mode flux [9]. Both of these geometries were originally constructed with two pieces such that there is only an air-gap at the top. The dual air-gap shown in Figure 4 is introduced in this work. The third geometry is basically an EE-Core but instead of one central

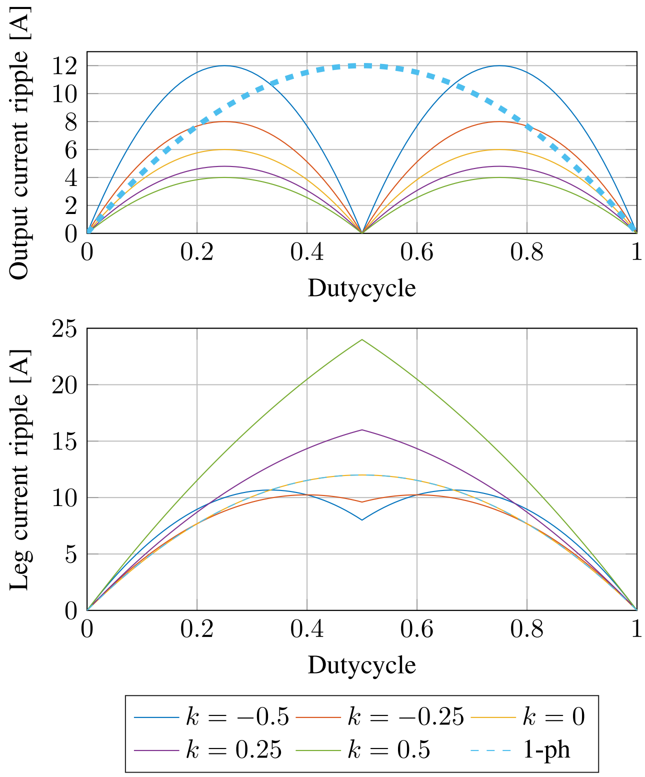

Fig. 5: Output current ripple and leg ripple for different coupling factors and constant input voltage. 1-ph for comparison. ToDo: Redo with normalized y-axis.

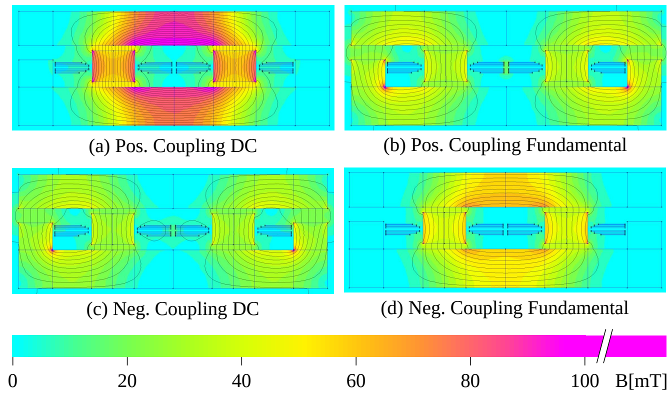

Fig. 6: Flux-Distribution for negative and positive coupling of otherwise identical designs for a DC phase current of 40 A and 100 A of ripple.

gap, two gaps are used. Lastly, the vertical gap geometry proposed by [7] is investigated which can partly compensate the internal proximity effect.

All designs use a single turn with all six layers in parallel which is very different from their original designs. Six layers were chosen due to the significantly cheaper manufacturing cost compared to higher layer counts. The inner layers have a thickness of $70\,\mu\mathrm{m}$ while the outer ones have only $35\,\mu\mathrm{m}$, due to the tight spacing of the selected gate-driver which required a $35\,\mu\mathrm{m}$ outer layer at the selected manufacturer to meet clearance constraints. Designs with more than one turn were not considered because the desired inductance and coupling-factor could not be achieved in that case due to fringing.

b) Material limitations: High-frequency ferrite materials for power applications have some unique properties that differ from those for lower frequency applications. TDK's PC200 was selected for this design as it exhibits very low loss in the range of 1 to $4\,\mathrm{MHz}$. However, the performance of PC200 significantly degrades for a field strength $H_{\mathrm{dc}} > 50\,\mathrm{A/m}$ and at $H_{\mathrm{dc}} > 100\,\mathrm{A/m}$ its losses double[1] [13]. Therefore, the inductor was designed with a maximum H_{dc} of $40\,\mathrm{A/m}$ to have some margin.

c) Positive vs negative coupling: Equation (4) and (5) are plotted in Figure 5 for positive and negative coupling-factors. While a strong positive coupling decreases ΔI_{out} it increases ΔI_{leg}. This is intuitive when looking at Equation (2): A positive coupling factor shifts inductance from the magnetizing to the output inductance, resulting in lower output current ripple but higher magnetizing current ripple. This means positive coupling require a larger L_{self} to achieve the same I_{on} if all other parameters remain the same.

Overall, positive coupling is slightly beneficial from an electrical point of view as it allows the usage of a larger L_{self} resulting in very low ΔI_{out}. However, in order to increase L_{self}, the air-gap has to be reduced, resulting in a higher flux-density and consequently higher core-losses or the number of windings has to be increased resulting in higher copper-loss. Furthermore, there is a very notable difference in the flux distribution as shown in Figure 6: For negative coupling, the two windings generate an opposing magnetomotive force at DC, resulting in a low flux and that circulates through the outer air-gaps. For positive coupling, the two magnetomotive forces are driving a DC-flux in the same direction causing a large flux that only circulates between the two windings where the reluctance is much lower. The peak flux-density is almost three times higher for positive coupling and as the core should be designed with respect to the H_{dc} limit, this means thicker top and bottom areas would be needed. Therefore, negative coupling is selected for this application[2]. For the fundamental (and all other odd harmonics), the flux-paths are swapped compared to DC (and even harmonics) as shown in 6c) and d).

d) Simulation Process: For the simulation, the open-source 2D FEM software FEMM was used due to its high speed and easy integration with Matlab. As the core-structures are neither planar nor axisymmetric, the designs were first transformed to a planar structure. All cross-sectional areas are kept the same and the depth of the design is determined by

[1]This effect is even more pronounced in NiZn materials which can be permanently damaged by large fields.

[2]Note that for lower frequency materials which are less affected by DC flux, the picture would change: Those designs would likely benefit from positive coupling as the flux-density at the fundamental is reduced.

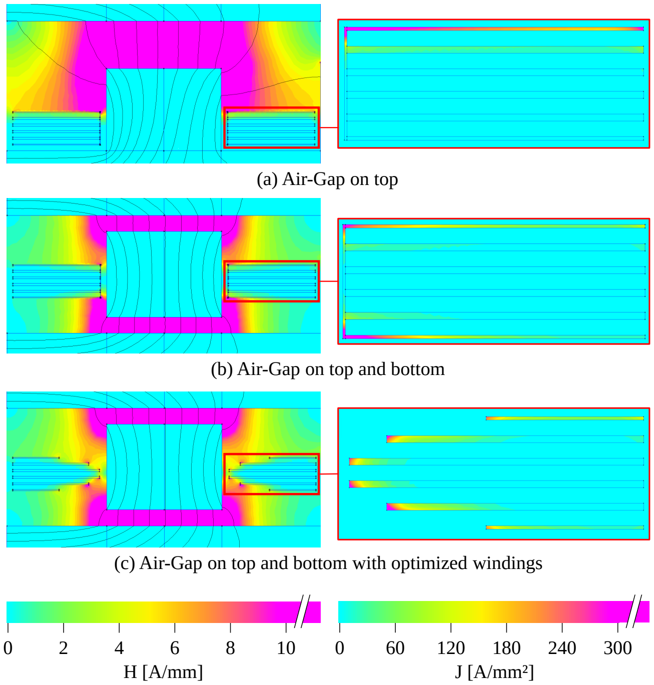

(a) Air-Gap on top

(b) Air-Gap on top and bottom

(c) Air-Gap on top and bottom with optimized windings

Fig. 7: Field and current distribution for different approaches. Because all layers are in parallel the current crowds in areas of large field-strength. By splitting the gap, the field gets distributed more evenly and the current distribution improves. Utilizing a smaller width for the outer layers, i.e. moving the copper away from the high-flux areas distributes the current even better.

TABLE I: Comparison of the size and loss of the optimized pillar and windings for the four-pole design.

	Volume [cm^3]	Copper Loss [W]
Original design	5.8	7.0
Air-Gap on top and bottom	5.5	5.7
Air-Gap on top and bottom, curved windings	5.3	5.0

the length of the winding[3].

For validation, the design was also transformed into an axisymmetric structure (neglecting the effects of coupling). This has the advantage that the current distribution and consequently copper-loss is closer to reality at the expense of less-precise core-loss.

e) Split air-gap and optimized windings: The external proximity effect caused by the air-gap plays an important role for the current distribution and consequently the losses of this high-frequency inductor. The field-strength at the top of the windings is large and almost zero at the bottom. As a result, the AC current is only flowing in the top layers. By centering the pillar vertically in the window such that there is an equal air-gap on the top and on the bottom, the field-strength is distributed much more uniformly and current flows in the top and bottom layers. This results in a $20\,\%$ reduction in losses, which can be reduced even further by using curved windings

[3]As the current does not flow in the middle of the winding but closer to its center due to the shorter length and the magnetic field, the circumference taken not from the middle of the winding but closer to the inside

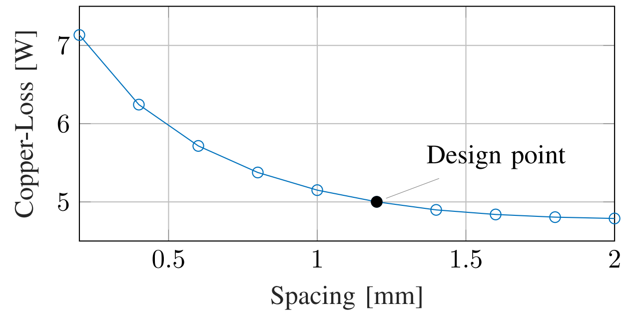

Fig. 8: Spacing between PCB and core vs. loss for the four-pole core (with curved windings and centered pillar). The distance between the PCB and the side air-gap core is fixed to $0.2\,\mathrm{mm}$ and the distance between PCB and bottom is varied. The pillar is always centered between top and bottom. ToDO: Add curve for total volume.

TABLE II: Comparison of the size and loss of the different core structures for $1.5\,\mathrm{MHz}$ respecting the H_{dc} limit.

	Total Area [cm^2]	Height [cm]	Volume [cm^3]	Copper Loss [W]
Four-Pole	5.5	0.9	5.3	5.0
Double PQ	6.2	0.9	5.5	5.2
Vertical gap	8.0	0.7	5.8	5.6
UU core	8.1	1.1	8.9	6.0

as shown in Table I.

f) Inductor Design Process: A manual optimization was conducted for each structure. The desired switching-frequency was fixed to $1.5\,\mathrm{MHz}$ for full-load operation, the coupling-factor to -0.3, and the winding with to $3\,\mathrm{mm}$ as this showed a good balance between size and losses. The cross-sectional areas were designed to result in $H_{\mathrm{dc}} \leq 40\,\mathrm{A/m}$ and the air-gaps are defined by desired inductance (i.e. switching frequency) and coupling-factor. The spacing between PCB and top/bottom of the core is the only free variable and has to be chosen for a compromise between size and efficiency.

g) Vertical Air-Gap: The design with vertical air-gap showed a significantly lower loss compared to a traditional horizontal gap while having a much lower volume. This confirms the results from [7]. The main downside of this design is the significant external field on top and bottom of the inductor. This makes cooling difficult as no conductive material can be placed on top or bottom of the core, eliminating one of the typical advantages of planar inductors: The large area for cooling. Cooling from the side is proposed by [7] by having copper extending to the outside of the core where a heatsink can be attached but this is much less convenient and requires additional space.

h) Comparison of Core Structures: A comparison of the core structures is shown in Table II. All designs except the one with vertical gap use the optimized curved windings. The four-pole structure showed the lowest losses and volume and was chosen for the implementation. The inductor design is shown in figure 9.

IV. Experimental Prototype

The assembled prototype is shown in Figure 10. The boxed volume of just $12.4\,\mathrm{cm}^3$ results in a powder density of

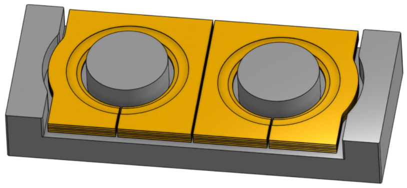

Fig. 9: Final design of the four-pole inductor; top-piece not shown.

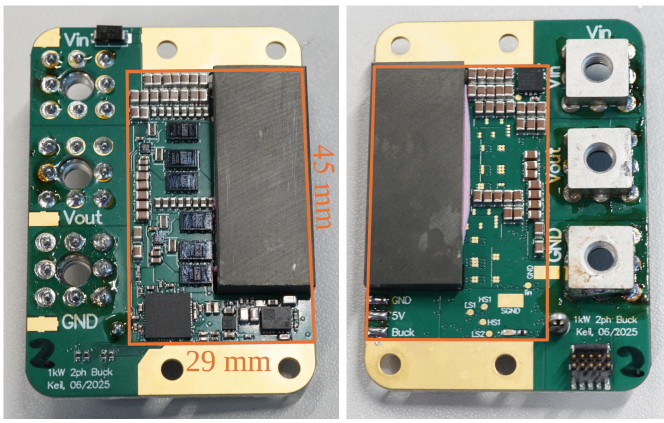

Fig. 10: Fully assembled prototype (without heatspreader). The converter area shown in orange is 45 x 29 x 9.5 mm. Outside of this area only the connectors for power and programming are placed as well as a protection diode and the programming resistors. ToDo: White Background and place match next to it.

$80\,\mathrm{kW/L}$ ($1300\,\mathrm{W/in^3}$). It's main hardware components are listed in table III. Two parallel low side transistors per phase are used as the converter operates at a low dutycycle. To minimize the stray inductance, the decoupling capacitors for the half-bridges were connected to the devices with a vertical power-loop layout which uses the first inner layer as a return path as proposed by [14]. In contrast to other designs, the large onboard capacitance allows the converter to operate without any additional off-board capacitance.

The converter operates over the entire range as expected. The efficiency is shown in Figure 11 which reaches its maximum of $96.3\,\%$ at around $550\,\mathrm{W}$, demonstrating the efficacy of the inductor structure.

V. Conclusion

ToDo

A more detailed analysis of the losses will be given in the final paper including a calculation of the ratio of different loss-mechanisms.

TABLE III: Overview of the main hardware components.

Component	Description
C_{in}	44x $2.2\,\mu\mathrm{F}$ $100\,\mathrm{V}$ X7R ($20\,\mu\mathrm{F}$ at $48\,\mathrm{V}$)
C_{out}	16x $2.2\,\mu\mathrm{F}$ $100\,\mathrm{V}$ X7R ($33\,\mu\mathrm{F}$ at $12\,\mathrm{V}$)
GaN-FETs	Infineon IGC025S08S1
Gate Driver	Analog Devices LT8418
Microcontroller	Texas Instruments F280049C
Aux. Power Supply	Texas Instruments TPSM365R6
Current Sensor	Allegro ACS37220

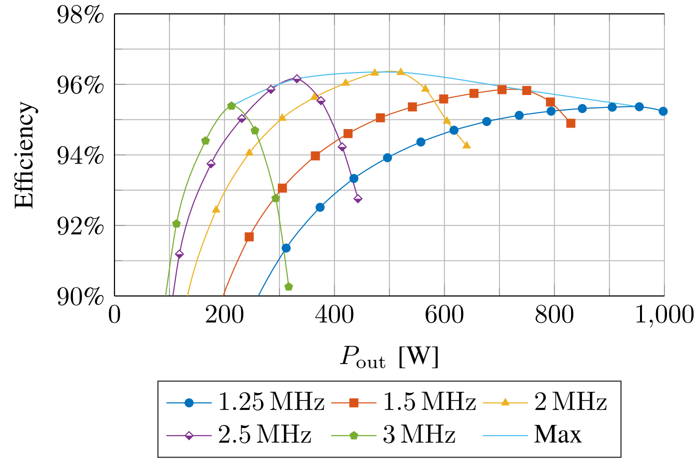

Fig. 11: Efficiency of the prototype for $V_{\mathrm{in}} = 48\,\mathrm{V}$ and $D = 0.25$.

References

[1] A. K. Kumawat and A. K. Thakur, “A Comprehensive Study of Automotive 48-Volt Technology,” *International Journal of Mechanical Engineering*, vol. Volume 4, Jan. 2019, publisher: SSRG International Journal. [Online]. Available: https://www.internationaljournalssrg.org/IJME/paper-details?Id=73

[2] N. Weitz, S. Ehrlich, P. Freundl, J. Schültzke, and M. März, “A High Frequency Resonant Push-Pull Converter with a Single Integrated Magnetic Component,” in *2023 IEEE Applied Power Electronics Conference and Exposition (APEC)*, Mar. 2023, pp. 435–440, iSSN: 2470-6647. [Online]. Available: https://ieeexplore.ieee.org/document/10131366

[3] Y. Wang, O. Lucia, Z. Zhang, S. Gao, Y. Guan, and D. Xu, “A Review of High Frequency Power Converters and Related Technologies,” *IEEE Open Journal of the Industrial Electronics Society*, vol. 1, pp. 247–260, 2020. [Online]. Available: https://ieeexplore.ieee.org/document/9195796

[4] C. Marxgut, J. Biela, and J. W. Kolar, “Interleaved Triangular Current Mode (TCM) resonant transition, single phase PFC rectifier with high efficiency and high power density,” in *The 2010 International Power Electronics Conference - ECCE ASIA -*, Jun. 2010, pp. 1725–1732. [Online]. Available: https://ieeexplore.ieee.org/document/5542048

[5] S. Wang, P. H. Pham, Q. Li, A. Nabih, and P. R. Prakash, “PCB Winding-Based Coupled Inductor for a High-Frequency DC/DC Converter with 99% Efficiency,” in *2023 IEEE Applied Power Electronics Conference and Exposition (APEC)*, Mar. 2023, pp. 420–425, iSSN: 2470-6647. [Online]. Available: https://ieeexplore.ieee.org/document/10131439

[6] B. Li, W. Qin, Y. Yang, Q. Li, F. C. Lee, and D. Liu, “A High Frequency High Efficiency GaN Based Bi-Directional 48V/12V Converter with PCB Coupled Inductor for Mild Hybrid Vehicle,” in *2018 IEEE 6th Workshop on Wide Bandgap Power Devices and Applications (WiPDA)*, Oct. 2018, pp. 204–211. [Online]. Available: https://ieeexplore.ieee.org/document/8569067

[7] J. Schäfer, D. Bortis, and J. W. Kolar, “Novel Highly Efficient/Compact Automotive PCB Winding Inductors Based on the Compensating Air-Gap Fringing Field Concept,” *IEEE Transactions on Power Electronics*, vol. 35, no. 9, pp. 9617–9631, Sep. 2020, conference Name: IEEE Transactions on Power Electronics. [Online]. Available: https://ieeexplore.ieee.org/document/8968357

[8] Y. Cai, M. H. Ahmed, Q. Li, and F. C. Lee, “Optimal Design of Megahertz LLC Converter for 48-V Bus Converter Application,” *IEEE Journal of Emerging and Selected Topics in Power Electronics*, vol. 8, no. 1, pp. 495–505, Mar. 2020. [Online]. Available: https://ieeexplore.ieee.org/document/8823928

[9] M. Hua, J. Chen, G. Xu, and H. Wu, “Ultra-thin Coupled Inductor for a GaN-Based CRM Buck Converter,” in *2021 IEEE Workshop on Wide Bandgap Power Devices and Applications in Asia (WiPDA Asia)*, Aug. 2021, pp. 138–142. [Online]. Available: https://ieeexplore.ieee.org/document/9656036/citations#citations

[10] C. Nan and R. Ayyanar, “A 1 MHz bi-directional soft-switching DC-DC converter with planar coupled inductor for dual voltage automotive

systems," in *2016 IEEE Applied Power Electronics Conference and Exposition (APEC)*, Mar. 2016, pp. 432–439. [Online]. Available: https://ieeexplore.ieee.org/abstract/document/7467908

[11] Y. Dong, "Investigation of Multiphase Coupled-Inductor Buck Converters in Point-of-Load Applications," Jul. 2009, publisher: Virginia Tech. [Online]. Available: http://hdl.handle.net/10919/28469

[12] D. Sha, Y. Zhao, and D. Zhang, "ZVS-Interleaved Synchronous Buck DC–DC Converter With a Coupled Inductor by Varying Switching Frequency and Deadtime," *IEEE Transactions on Power Electronics*, vol. 37, no. 7, pp. 8190–8198, Jul. 2022, conference Name: IEEE Transactions on Power Electronics. [Online]. Available: https://ieeexplore.ieee.org/abstract/document/9674799

[13] TDK, "High-Frequency, Low-Loss Ferrite Material PC200." [Online]. Available: https://product.tdk.com/de/techlibrary/productoverview/ferrite_pc200.html

[14] D. Reusch and J. Strydom, "Understanding the Effect of PCB Layout on Circuit Performance in a High-Frequency Gallium-Nitride-Based Point of Load Converter," *IEEE Transactions on Power Electronics*, vol. 29, no. 4, pp. 2008–2015, Apr. 2014. [Online]. Available: https://ieeexplore.ieee.org/document/6531683